2020 IEEE International Conference on Robotics and Automation (ICRA)
31 May - 31 August, 2020. Paris, France

Observability Analysis of Flight State Estimation for UAVs and Experimental Validation

Peng Huang[1], Heinrich Meyr[2], Meik Dörpinghaus[1], and Gerhard Fettweis[1,2]

***Abstract*— UAVs require reliable, cost-efficient onboard flight state estimation that achieves high accuracy and robustness to perturbation. We analyze a multi-sensor extended Kalman filter (EKF) based on the work by Leutenegger. The EKF uses measurements from a MEMS-based inertial system, static and dynamic pressure sensors as well as GPS. As opposed to other implementations we do not use a magnetic sensor because the weak magnetic field of the earth is subject to disturbances. Observability of the state is a necessary condition for the EKF to work. In this paper, we demonstrate that the system state is observable – which is in contrast to statements in the literature – if the random nature of the air mass is taken into account. Therefore, we carry out an in-depth observability analysis based on a singular value decomposition (SVD). The numerical SVD delivers a wealth of information regarding the observable (sub)spaces. We validated the theoretical findings based on sensor data recorded in test flights on a glider. Most importantly, we demonstrate that the EKF works. It is capable of absorbing large perturbations in the wind state variable converging to the undisturbed estimates.**

I. Introduction

Unmanned aerial vehicles (UAVs) require reliable, cost-efficient onboard flight state estimation that achieves high accuracy as well as robustness to certain perturbation. We analyze a multi-sensor extended Kalman filter (EKF) based on the work by Leutenegger [1], [2], [3]. The EKF uses measurements from a micro-electro-mechanical system (MEMS) based inertial system, static and dynamic pressure sensors, as well as GPS and a magnetic sensor. We briefly summarize the features of the EKF.

In the EKF introduced by Leutenegger, the position, the orientation, the ground speed, inertial measurement unit (IMU) biases, and the wind are included in the state vector. Measurement updates are initiated by the GPS, the magnetometer, and the pressure sensors. In addition, the framework employs an aerodynamic model of the lateral force and the speed polar to generate residuals, which update the state to obtain accurate 3D wind, sideslip angle, and angle of attack estimates.

It is frequently argued that a magnetometer is necessary for the estimation of the flight state [1], [2], [3], [4]. This conclusion is easily understandable by looking at the wind triangle for constant wind and constant ground speed. If only the quadratic measure of true airspeed provided by the Pitot tube is available it is not possible to determine the wind vector. To resolve the phase ambiguity a magnetic sensor, a dual GPS, or other additional sensors to obtain the wind angles [5], [6] are required. However, these sensors have severe deficits for use in UAVs or gliders. The weak magnetic field measured by a magnetic sensor is subject to static and dynamic disturbances. These disturbances are difficult to calibrate, if at all. The alternative is expensive mounting away from the disturbances. The dual GPS requires elaborate electrical installations. The disadvantages of these sensors make their use in most UAV and glider applications infeasible.

For the above reasons, it is therefore of practical and theoretical interest to investigate the conditions under which the EKF works without a magnetometer. The work described in this paper was inspired by the fact that well-known algorithms for wind measurements function during circling. Our early experiments also demonstrated that the EKF works – under certain conditions on the dynamics of the random flight trajectory – without a magnetometer.

Observability deals with the question whether it is possible to reconstruct the states of a dynamic system from available measurements. Clearly, if certain states are not observable the EKF cannot estimate these states. Thus, the observability of the system state is a necessary condition for the EKF to work. For linear systems, the state is observable if the observability matrix has full rank. For nonlinear systems, the nonlinearity introduces difficulties requiring advanced mathematical tools, such as Lie derivatives [7]. Martinelli [8] used Lie derivatives to analyze the observability of a nonlinear navigation system based on time-continuous state equations. Alternatively, one can carry out the observability analysis by linearization of the nonlinear time-varying system around a nominal trajectory [9], [10], [11]. Similarly, we approximate the presented system by a discrete-time, time-varying system. The sampling rates of the sensor signals are 10-100 Hz, which is at least 1-2 orders of magnitude larger than the inverse of the dominant time constant of the UAV. Hence, the discrete-time system operates quasi-time continuous. We linearize the state equations around a nominal trajectory to obtain a discrete-time, linear system. This approach is justified since the EKF uses a similar approximation. The contribution of this paper is to demonstrate that the state is observable (contrary to statements in the literature) if the random nature of the air mass is mathematically taken into account.

Our mathematical analysis is an in-depth observability analysis based on a singular value decomposition (SVD). The numerical SVD delivers much more than a rank test. A wealth of information can be deduced regarding the

This work was supported by the Deutsche Forschungsgemeinschaft (DFG, German Research Foundation) under grant FE 423/20-1.

[1]Vodafone Chair Mobile Communications Systems, Technische Universität Dresden, 01062 Dresden, Germany, {peng.huang, meik.doerpinghaus, gerhard.fettweis}@tu-dresden.de

[2]Barkhausen Institut, 01062 Dresden, Germany, meyr@iss.rwth-aachen.de

observable (sub)spaces by inspection of the singular vector associated with a singular value [12]. We validated the theoretical findings in an extensive series of test flights on a glider. The sensor signals were recorded during the flights and later analyzed in a tool suite on the ground. We performed a numerical observability analysis, which confirmed our theoretical findings. Most importantly, we demonstrate that the EKF works without a magnetic sensor. It is capable of absorbing large perturbations in the wind state variable converging to the undisturbed estimates.

The paper is organized as follows. Section II provides an overview of the system model. For this purpose, we first describe the system by its kinematic equations including the wind model and modeling of sensor biases. We briefly describe the considered EKF based flight state estimator, which is closely related to the EKF introduced by Leutenegger. In Section III, to get a basic understanding of the system behavior it proved to be useful to analyze a simplified 2D EKF, which just considers the position, ground speed, and wind speed in the horizontal plane and which can also be handled analytically. We carried out an observability analysis for the simplified 2D EKF yielding the key contribution of the paper, a condition under which the system without a magnetometer is observable. We show that the state is observable in case of a varying direction of the true airspeed, a condition that is fulfilled in practical scenarios due to the random nature of the air mass. This result is followed by a detailed numerical study of the observable sub-spaces for different flight paths based on an SVD of the observability matrix. Subsequently, in Section IV the numerical observability analysis based on the SVD is also carried out for the full state EKF showing that the state is effectively observable without a magnetic sensor. Thereafter, in Section V we experimentally validated our theoretical results. More specifically, we tested the 2D EKF with simulated flight trajectories and we tested the full state EKF using data recorded in an extensive series of test flights on a glider. These experiments, on the one hand, confirmed the results of the observability analysis and, on the other hand, demonstrated that the EKF works. Finally, Section VI gives a conclusion and discusses some future work.

Notation: Vectors and matrices are set in bold font. The superscript T denotes a transpose. Measurements are denoted by a tilde, e.g., $\tilde{p}_d$ and estimates are denoted by hats, e.g., $\hat{\boldsymbol{r}}$. Dots denote time derivatives, e.g., $\dot{\boldsymbol{r}}$.

II. Flight State Estimation

Fig. 1 provides an overview of the input and output quantities of the EKF flight state estimation. The purpose of the EKF is to estimate the 3D position $\boldsymbol{r}$, the 3D ground speed ${}_N\boldsymbol{v}$, the orientation given by the 4D quaternion $\boldsymbol{q}_{NB}$, and the 3D wind speed ${}_N\boldsymbol{d}$. Hence, all these quantities are included in the state vector of the EKF. As the measurements of the gyro and the accelerometer are strongly biased, these biases $\boldsymbol{b}_g$ and $\boldsymbol{b}_a$ are also tracked by the EKF and, thus, included in the state vector, which is then given by

$$\boldsymbol{x} = \begin{bmatrix} \boldsymbol{r}^{\mathrm{T}} & {}_N\boldsymbol{v}^{\mathrm{T}} & \boldsymbol{q}_{NB}^{\mathrm{T}} & {}_N\boldsymbol{d}^{\mathrm{T}} & \boldsymbol{b}_g^{\mathrm{T}} & \boldsymbol{b}_a^{\mathrm{T}} \end{bmatrix}^{\mathrm{T}} \in \mathbb{R}^{19}. \quad (1)$$

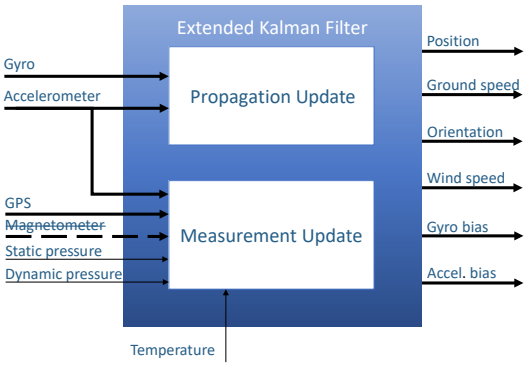

Fig. 1. Flight state estimation fusing information from various sensors.

Here, the subscripts N and B denote the north-east-down (NED) and the body frame, respectively. Moreover, $\boldsymbol{q}_{NB}$ represents the orientation of the body frame with respect to the NED frame. The position $\boldsymbol{r}$ is given in terms of the latitude ϕ, the longitude λ, and the altitude h. Note that the state vector has 19 dimensions, which however could be reduced to 18 since the Euclidean norm of the quaternion is one [13].

The flight state estimation is based on the following measurements acting as inputs to the EKF: the angular rate ${}_B\tilde{\boldsymbol{\omega}}$, the acceleration ${}_B\tilde{\boldsymbol{a}}$, the GPS position $\tilde{\boldsymbol{r}}$, the static pressure $\tilde{p}_s$, the dynamic pressure $\tilde{p}_d$, and the temperature $\tilde{T}$. As motivated before, we do not use the magnetometer as the magnetic field of the earth is easily disturbed onboard of UAVs, e.g., by electronic equipment.

In the following, for the sake of readability, we briefly describe the EKF based on the work by Leutenegger [2]. Each iteration of the EKF consists of two steps, the propagation update and the measurement update. In the propagation step, the states are predicted based on the following model equations describing time-derivatives of the states [2], [6], [13]:

$$\dot{\boldsymbol{r}} = \operatorname{diag}\begin{bmatrix} \frac{1}{R_\phi + h} & \frac{1}{(R_\lambda + h)\cos(\phi)} & -1 \end{bmatrix} {}_N\boldsymbol{v}, \quad (2)$$

$${}_N\dot{\boldsymbol{v}} = \boldsymbol{C}_{NB}({}_B\tilde{\boldsymbol{a}} - \boldsymbol{b}_a - \boldsymbol{w}_a) + {}_N\boldsymbol{g}, \quad (3)$$

$$\dot{\boldsymbol{q}}_{NB} = \tfrac{1}{2}\boldsymbol{q}_{NB} \otimes ({}_B\tilde{\boldsymbol{\omega}} - \boldsymbol{b}_g - \boldsymbol{w}_g), \quad (4)$$

$${}_N\dot{\boldsymbol{d}} = \boldsymbol{w}_d, \quad (5)$$

$$\dot{\boldsymbol{b}}_g = \boldsymbol{w}_{b_g}, \quad (6)$$

$$\dot{\boldsymbol{b}}_a = -\tfrac{1}{\tau}\boldsymbol{b}_a + \boldsymbol{w}_{b_a}. \quad (7)$$

Here R_ϕ and R_λ denote local radii of the Earth [14, p. 41], ${}_N\boldsymbol{g}$ denotes the gravity field vector in the NED frame, $\boldsymbol{C}_{NB}$ is the coordinate transformation matrix from the body frame to the NED frame, τ is the time constant of the change of the accelerometer bias, and $\otimes$ is quaternion multiplication [13]. Moreover, the acceleration, the angular rate, the wind, the bias of the gyro, and the bias of the accelerometer are modeled as Brownian processes. We define the vector $\boldsymbol{w}$ containing the corresponding system noise processes as $\boldsymbol{w} = \begin{bmatrix} \boldsymbol{w}_a^{\mathrm{T}} & \boldsymbol{w}_g^{\mathrm{T}} & \boldsymbol{w}_d^{\mathrm{T}} & \boldsymbol{w}_{b_g}^{\mathrm{T}} & \boldsymbol{w}_{b_a}^{\mathrm{T}} \end{bmatrix}^{\mathrm{T}}$. All these noise processes are white Gaussian and mutually independent. Note that the measurements of the acceleration and the angular rate feed the system dynamical model in the propagation step. The system transition matrix is calculated

by linearizing the continuous-time system (2)-(7) based on the error state estimates [13]

$$\boldsymbol{F}_c = \begin{bmatrix} \mathbf{0}_{3\times3} & \boldsymbol{F}_{1,2} & \mathbf{0}_{3\times3} & \mathbf{0}_{3\times3} & \mathbf{0}_{3\times3} & \mathbf{0}_{3\times3} \\ \mathbf{0}_{3\times3} & \mathbf{0}_{3\times3} & \boldsymbol{F}_{2,3} & \mathbf{0}_{3\times3} & \mathbf{0}_{3\times3} & -\hat{\boldsymbol{C}}_{NB} \\ \mathbf{0}_{3\times3} & \mathbf{0}_{3\times3} & \boldsymbol{F}_{3,3} & \mathbf{0}_{3\times3} & -\mathbf{I}_{3\times3} & \mathbf{0}_{3\times3} \\ \mathbf{0}_{3\times3} & \mathbf{0}_{3\times3} & \mathbf{0}_{3\times3} & \mathbf{0}_{3\times3} & \mathbf{0}_{3\times3} & \mathbf{0}_{3\times3} \\ \mathbf{0}_{3\times3} & \mathbf{0}_{3\times3} & \mathbf{0}_{3\times3} & \mathbf{0}_{3\times3} & \mathbf{0}_{3\times3} & \mathbf{0}_{3\times3} \\ \mathbf{0}_{3\times3} & \mathbf{0}_{3\times3} & \mathbf{0}_{3\times3} & \mathbf{0}_{3\times3} & \mathbf{0}_{3\times3} & -\frac{1}{\tau}\mathbf{I}_{3\times3} \end{bmatrix} \tag{8}$$

with the non-zero elements

$$\begin{aligned} \boldsymbol{F}_{1,2} &= \operatorname{diag}\begin{bmatrix} \frac{1}{R_\phi+\hat{h}} & \frac{1}{(R_\lambda+\hat{h})\cos(\hat{\phi})} & -1 \end{bmatrix}, \\ \boldsymbol{F}_{2,3} &= -\hat{\boldsymbol{C}}_{NB}[{}_B\tilde{\boldsymbol{a}} - \hat{\boldsymbol{b}}_a]_\times, \\ \boldsymbol{F}_{3,3} &= -[{}_B\tilde{\boldsymbol{\omega}} - \hat{\boldsymbol{b}}_g]_\times, \end{aligned} \tag{9}$$

where $[\bullet]_\times$ is the cross product matrix. Note, $\boldsymbol{F}_c$ is of size 18×18 as we reduced the state vector by one dimension by linearizing the quaternion by small angular perturbation [13].

The measurement update corrects the predicted states based on the residuals for the GPS position $\boldsymbol{r}$, the static pressure p_s, and the dynamic pressure p_d which are given by

$$\boldsymbol{e}_r = \tilde{\boldsymbol{r}} - \boldsymbol{r}, \tag{10}$$

$$e_s = \tilde{p}_s - p_s = \tilde{p}_s - p_0\left(1 - \frac{L_0(h-N)}{\tilde{T}}\right)^l, \tag{11}$$

$$e_d = \tilde{p}_d - p_d = \tilde{p}_d - \tfrac{1}{2}\rho_B v_{tx}^2, \tag{12}$$

where p_0 is the pressure at mean sea level, L_0 is the temperature lapse rate, l is a constant from a standard atmospheric model, N is the geoid height [14, p. 230], and ρ denotes the air density. Finally, ${}_Bv_{tx}$ is the x-component of the true airspeed in the body frame, i.e., the component along the longitudinal axis of the UAV. The true airspeed can be derived via the wind triangle ${}_N\boldsymbol{v}_t = {}_N\boldsymbol{v} - {}_N\boldsymbol{d}$.

To estimate the 3D wind vector while having only a 1D measurement of the true airspeed, i.e., the magnitude provided by the dynamic pressure sensor, we use two aerodynamic constraints of fixed-wing airplanes as residuals. The first constraint is the side force Y that acts on the lateral surface of the aircraft, mainly on the vertical tail, due to the oncoming air [3], [15, p. 60] (see Fig. 2). The second constraint characterizes the sink rate v_d as a function of the forward true airspeed in Fig. 3. These aerodynamic constraints yield the following residuals [3]

$$e_Y = \tilde{Y} - Y = m({}_B\tilde{a}_y - b_{a,y}) - p_d S C_Y, \tag{13}$$

$$e_{v_d} = a_2 {}_Bv_{tx}^2 + a_1 {}_Bv_{tx} + a_0 + {}_B\boldsymbol{v}_t^{\mathrm{T}}\boldsymbol{\Pi}_l \boldsymbol{n}({}_B\tilde{\boldsymbol{a}} - \boldsymbol{b}_a). \tag{14}$$

Here S is the wing area, C_Y is the side force coefficient approximately proportional to the sideslip angle β [15, p. 61], m is the mass of the UAV, and a_0, a_1 and a_2 are constants of the speed polar. Here $\boldsymbol{\Pi}_l = \operatorname{diag}([1, 0, 1])$ is a projection matrix, and $\boldsymbol{n}(\boldsymbol{a})$ normalizes an arbitrary vector $\boldsymbol{a}$ to unit length.

Using (10) to (14) we get the following measurement matrix

$$\boldsymbol{H} = \begin{bmatrix} \mathbf{I}_{3\times3} & \mathbf{0}_{3\times3} & \mathbf{0}_{3\times3} & \mathbf{0}_{3\times3} & \mathbf{0}_{3\times3} & \mathbf{0}_{3\times3} \\ \begin{bmatrix}0 & 0 & \frac{\partial p_s}{\partial \hat{h}}\end{bmatrix} & \mathbf{0}_{1\times3} & \mathbf{0}_{1\times3} & \mathbf{0}_{1\times3} & \mathbf{0}_{1\times3} & \mathbf{0}_{1\times3} \\ \mathbf{0}_{1\times3} & \frac{\partial p_d}{\partial {}_N\boldsymbol{v}} & \frac{\partial p_d}{\partial \Delta\boldsymbol{\varphi}} & \frac{\partial p_d}{\partial {}_N\boldsymbol{d}} & \mathbf{0}_{1\times3} & \mathbf{0}_{1\times3} \\ \mathbf{0}_{1\times3} & \frac{\partial Y}{\partial {}_N\boldsymbol{v}} & \frac{\partial Y}{\partial \Delta\boldsymbol{\varphi}} & \frac{\partial Y}{\partial {}_N\boldsymbol{d}} & \mathbf{0}_{1\times3} & -\frac{\partial e_Y}{\partial \boldsymbol{b}_a} \\ \mathbf{0}_{1\times3} & -\frac{\partial e_{v_d}}{\partial {}_N\boldsymbol{v}} & -\frac{\partial e_{v_d}}{\partial \Delta\boldsymbol{\varphi}} & -\frac{\partial e_{v_d}}{\partial {}_N\boldsymbol{d}} & \mathbf{0}_{1\times3} & -\frac{\partial e_{v_d}}{\partial \boldsymbol{b}_a} \end{bmatrix}, \tag{15}$$

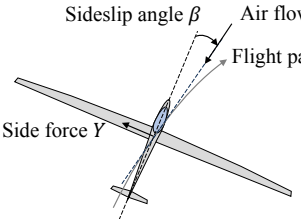

Fig. 2. Sideslip

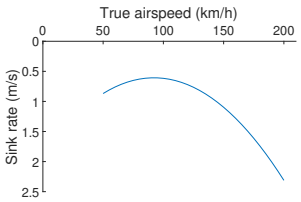

Fig. 3. Speed polar

where $\Delta\boldsymbol{\varphi}$ denotes the small angular variation [13]. Note that the residuals for static and dynamic pressure in (11) and (12) as well as the speed polar in (14) are nonlinear, rendering the measurement matrix to be time dependent.

The implementation of the flight state estimator in the EKF is based on a time discretization of the system model given by equations (2) to (14), where the sampling rate is chosen at least 1-2 orders of magnitude larger than the inverse of the relevant time constant of the UAV. Thus, we can linearize the state equations, the measurement equations, and the equations describing the aerodynamic constraints around the current state such that the system is modeled as linear time-variant.

III. Observability Analysis for a Simplified 2D Model

A. Simplified 2D Estimator

To get an in-depth understanding of the observability of the EKF based flight state estimation, we start with the analysis of a simplified 2D system model where the state vector is reduced to 6 dimensions. The simplified 2D EKF only estimates the 2D position ${}_N\boldsymbol{r}_k$, the 2D ground speed ${}_N\boldsymbol{v}_k$, and the 2D wind speed ${}_N\boldsymbol{d}_k$, which compose the state vector

$$\boldsymbol{x}_{2\mathrm{D},k} = \begin{bmatrix} {}_N\boldsymbol{r}_k^{\mathrm{T}} & {}_N\boldsymbol{v}_k^{\mathrm{T}} & {}_N\boldsymbol{d}_k^{\mathrm{T}} \end{bmatrix}^{\mathrm{T}}, \tag{16}$$

with time index k. These variables are given in the northeast domain, which is denoted by N in the present section. Their discrete-time kinematics are summarized by

$$\begin{aligned} {}_N\boldsymbol{r}_{k+1} &= {}_N\boldsymbol{r}_k + {}_N\boldsymbol{v}_k\Delta t, \\ {}_N\boldsymbol{v}_{k+1} &= {}_N\boldsymbol{v}_k + {}_N\boldsymbol{a}_k\Delta t, \\ {}_N\boldsymbol{d}_{k+1} &= {}_N\boldsymbol{d}_k + {}_N\boldsymbol{w}_{d,k}\Delta t, \end{aligned} \tag{17}$$

with ${}_N\boldsymbol{a}_k$ denoting the acceleration, ${}_N\boldsymbol{w}_{d,k}$ is the wind system noise, and Δt is the sampling time interval.

We consider a minimum set of measurements that consist of the GPS position ${}_N\boldsymbol{r}_k$ and the dynamic pressure $p_{d,k}$. Hence, the measurement model is given by

$$\boldsymbol{y}_{2\mathrm{D},k} = \begin{bmatrix} {}_N\boldsymbol{r}_k \\ p_{d,k} \end{bmatrix} + \boldsymbol{\nu}_{2\mathrm{D},k} = \begin{bmatrix} {}_N\boldsymbol{r}_k \\ \frac{1}{2}\rho({}_Nv_{tx,k}^2 + {}_Nv_{ty,k}^2) \end{bmatrix} + \boldsymbol{\nu}_{2\mathrm{D},k}, \tag{18}$$

where $\boldsymbol{\nu}_{2\mathrm{D},k}$ is white Gaussian noise of the observations with independent elements. In addition, ${}_Nv_{tx,k}$ and ${}_Nv_{ty,k}$ denote the true airspeed along the north and east direction, respectively. Here we assume that the pitch angle is small as in this case the horizontal true airspeed can be interpreted as the true airspeed along the longitudinal axis of the body frame.

B. Observability Analysis

Observability addresses the question whether the state of a system can be reconstructed from the measurement data. For a nonlinear system, the nonlinearity introduces substantial difficulties requiring advanced mathematical tools, such as Lie derivatives [7] for a continuous-time system. However, as stated above, the fact that the system is highly oversampled allows us to model it as a linear time-variant system. A linear system is observable if its observability matrix has full rank.

Consider a generic linear time-variant system:

$$\begin{aligned} \boldsymbol{x}_{k+1} &= \boldsymbol{F}_k \boldsymbol{x}_k + \boldsymbol{G}_k \boldsymbol{u}_k, \\ \boldsymbol{y}_k &= \boldsymbol{H}_k \boldsymbol{x}_k, \end{aligned} \tag{19}$$

with a state vector $\boldsymbol{x}_k$, an input vector $\boldsymbol{u}_k$, and an observation vector $\boldsymbol{y}_k$. Its observability matrix is given by [16, p. 467]

$$\boldsymbol{O} = \begin{bmatrix} \boldsymbol{H}_k \\ \boldsymbol{H}_{k+1}\boldsymbol{F}_k \\ \vdots \\ \boldsymbol{H}_{k+i-1}\boldsymbol{F}_{k+i-2}\boldsymbol{F}_{k+i-3}\dots\boldsymbol{F}_k \end{bmatrix}. \tag{20}$$

The state is observable in the time interval $[k, k+i]$ iff $\operatorname{rank}(\boldsymbol{O}) = n$ with n being the dimension of the state $\boldsymbol{x}_k$.

For the observability analysis we linearize the measurement equation (18) w.r.t. the states, yielding the measurement matrix $\boldsymbol{H}_k$. Subsequently, the observability matrix for the state in the 2D EKF is obtained as

$$\boldsymbol{O}_{2\mathrm{D}} = \begin{bmatrix} \boldsymbol{H}_k \\ \boldsymbol{H}_{k+1}\boldsymbol{F}_k \end{bmatrix} = \begin{bmatrix} \mathbf{I}_{2\times2} & \mathbf{0}_{2\times2} & \mathbf{0}_{2\times2} \\ \mathbf{0}_{1\times2} & \rho_N \boldsymbol{v}_{t,k}^{\mathrm{T}} & -\rho_N \boldsymbol{v}_{t,k}^{\mathrm{T}} \\ \mathbf{I}_{2\times2} & \mathbf{I}_{2\times2}\Delta t & \mathbf{0}_{2\times2} \\ \mathbf{0}_{1\times2} & \rho_N \boldsymbol{v}_{t,k+1}^{\mathrm{T}} & -\rho_N \boldsymbol{v}_{t,k+1}^{\mathrm{T}} \end{bmatrix}. \tag{21}$$

As the true airspeed vector cannot be zero, the minimum rank for the observability matrix (21) is 5 iff

$$\frac{\boldsymbol{v}_{ty,k+1}}{\boldsymbol{v}_{tx,k+1}} = \frac{\boldsymbol{v}_{ty,k}}{\boldsymbol{v}_{tx,k}}, \tag{22}$$

which corresponds to a straight motion. If the flight trajectory is curved, the rank of $\boldsymbol{O}_{2\mathrm{D}}$ becomes 6, i.e., the state becomes observable.

In case we have an additional measurement of the direction provided by a magnetometer perturbed by an additive noise

$$y_{m,k} = \psi_k + \nu_{m,k} = \arctan\left(\frac{{}_N v_{ty}}{{}_N v_{tx}}\right) + \nu_{m,k}, \tag{23}$$

with the heading ψ_k and the noise $\nu_{m,k}$, an additional row is added to the linearized measurement matrix $\boldsymbol{H}_k$

$$\boldsymbol{H}_{\psi,k} = \tfrac{1}{\|{}_N \boldsymbol{v}_t\|^2} \begin{bmatrix} 0 & 0 & -{}_N v_{ty,k} & {}_N v_{tx,k} & {}_N v_{ty,k} & -{}_N v_{tx,k} \end{bmatrix}. \tag{24}$$

The observability matrix has now dimension 8×6 and rank 6. The state is observable independent of the flight pattern.

C. Numerical Observability Analysis

In the following, we verify the observability condition (22) by calculating the singular values of the observability matrix via a singular value decomposition (SVD) for a simulated flight trajectory [17]. Moreover, the singular vectors given by the SVD enable to study the observable (sub)spaces [12], which we will discuss in detail. This gives deep insights into the behavior of the EKF based flight state estimation.

We briefly recall the essential properties of the SVD. Any $m \times n$ matrix $\boldsymbol{A}$ can be factored into [18, p. 331]

$$\boldsymbol{A} = \boldsymbol{U}\boldsymbol{\Sigma}\boldsymbol{V}^{\mathrm{T}} \tag{25}$$

with the $m \times m$ matrix $\boldsymbol{U}$ and the $n \times n$ matrix $\boldsymbol{V}$ being unitary. The left and right hand singular vectors of $\boldsymbol{A}$ are their columns, respectively. Moreover, the $m \times n$ matrix $\boldsymbol{\Sigma}$ is diagonal carrying the nonnegative singular values $\sigma_1, \sigma_2, \dots, \sigma_n$ of $\boldsymbol{A}$ on its main diagonal (assuming w.l.o.g. that $n \leq m$), which here are assumed to be sorted in decreasing order.

The matrices $\boldsymbol{A}$ and $\boldsymbol{\Sigma}$ describe the same mapping of a vector $\boldsymbol{x} \in \mathcal{X}$ to a vector $\boldsymbol{y} \in \mathcal{Y}$ in a different base system, where $\mathcal{X}$ and $\mathcal{Y}$ are vector spaces. The matrices $\boldsymbol{U}$ and $\boldsymbol{V}^{\mathrm{T}}$ define two base transformations. But why do we perform these two base transformation?

First, the fact that $\boldsymbol{\Sigma}$ is diagonal enables to easily test the rank of $\boldsymbol{A}$, which in our case is the observability matrix. $\boldsymbol{A}$ has full rank if $\sigma_i > 0$ for all $i \leq n$. Otherwise, it is rank deficient. The singular values calculated in a computer will not be exactly zero. Therefore, it is meaningful to speak of the effective rank of a matrix when we ignore all values below a given threshold which depends on the application.

Second, the SVD delivers much more than a rank test. A wealth of information can be deduced by inspection of the singular vector associated with a singular value based on the sum decomposition [18, p. 333]

$$\boldsymbol{A} = \boldsymbol{U}\boldsymbol{\Sigma}\boldsymbol{V}^{\mathrm{T}} = \sigma_1 \boldsymbol{u}_1 \boldsymbol{v}_1^{\mathrm{T}} + \sigma_2 \boldsymbol{u}_2 \boldsymbol{v}_2^{\mathrm{T}} + \dots + \sigma_n \boldsymbol{u}_n \boldsymbol{v}_n^{\mathrm{T}}. \tag{26}$$

Eq. (26) shows that any matrix can be expressed as the sum of rank 1 matrices. Geometrically, the space of dimension n is built up by n subspaces of dimension 1. Multiplying the matrix $\boldsymbol{A}$ with a right singular vector $\boldsymbol{v}_i$ produces a multiple of the column i of the matrix $\boldsymbol{U}$:

$$\boldsymbol{A}\boldsymbol{v}_i = \sigma_i \boldsymbol{u}_i \boldsymbol{v}_i^{\mathrm{T}} \boldsymbol{v}_i = \sigma_i \boldsymbol{u}_i. \tag{27}$$

From (27) it follows that every 1-dimensional subspace has n identical columns multiplied by the components of $\boldsymbol{V}^{\mathrm{T}}$. We also observe that the columns of the matrix $\boldsymbol{u}_i \boldsymbol{v}_i^{\mathrm{T}}$ are weighted by the singular value σ_i. Eq. (26) can be used as the basis of an approximation of the $\boldsymbol{A}$ with a rank k matrix, $\boldsymbol{A}^{(k)}$. Such an approximation is called a low rank approximation, which is optimal in the sense that it minimizes the quadratic Frobenius norm. Why is this approximation useful? This will be explained by an example of the simplified 2D system.

Using the framework in [17] based on a dynamic control algorithm for gliders, we generate simulated flight data, which has a straight flight and two banking turns. The wind is assumed constant. We assume $10^{-4}(\mathrm{m/s^2})^2/\mathrm{Hz}$ for the power spectral density (PSD) of the acceleration and $2.5 \times 10^{-3}(\mathrm{m/s^2})^2/\mathrm{Hz}$ for the PSD of the wind in the EKF. The standard deviations of the dynamic pressure noise and the horizontal components of the GPS position noise are given in Table I. Fig. 4a shows the singular values of the observability matrix of the simplified system in a straight flight. We observe a gap of approximately one order of magnitude between the two smallest singular values σ_5 and σ_6. This is typical for an effectively rank deficient matrix.

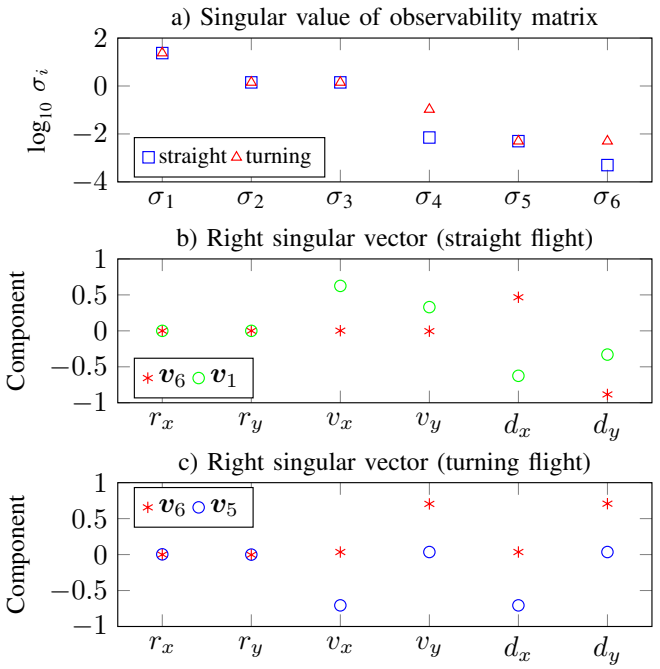

Fig. 4. SVD of the observability matrix for the 2D model: a) singular values in logarithmic scale in a straight and a turning flight, b) right singular vector $\boldsymbol{v}_6$ and $\boldsymbol{v}_1$ of the smallest and largest singular value in the straight flight, respectively, c) right singular vector $\boldsymbol{v}_5$ and $\boldsymbol{v}_6$ of the two smallest singular values in the turning flight, respectively.

If one ignores the contribution of the smallest singular value σ_6 the effective rank of the matrix is 5 and the matrix $\boldsymbol{O}_{2D}$ can be approximated by $\boldsymbol{O}_{2D}^{(5)}$. It is instructive to inspect the right singular vector $\boldsymbol{v}_6$ in Fig. 4b. Only the components of the north and east wind (d_x, d_y) are nonzero. Thus, a 1-dimensional subspace of the wind components is unobservable. If one sets $\sigma_6 = 0$ the vector $\boldsymbol{v}_6$ is mapped to a zero vector. Since the remaining four state variables (r_x, r_y, v_x, v_y) are in the nullspace of $\boldsymbol{v}_6$ these states can, in principle, be observed if the observable subspace has dimension 4. As the effective rank of $\boldsymbol{O}_{2D}$ is 5 a 1-dimensional subspace of the wind is still observable. This statement is supported by the fact that the 5th and 6th entry of $\boldsymbol{v}_1$, i.e., the singular vector of the largest singular value, are nonzero, see Fig. 4b. This observation corresponds to the intuition that based on the Pitot tube we can estimate the magnitude of the true airspeed, but not its direction, which leaves, in consequence, one degree of freedom for the wind estimate.

Another maneuver is turning. Fig. 4a also shows the singular values in a turning flight at an arbitrarily chosen time instant. Differently to the case of a straight flight the 5th and 6th singular value are equal, having the same value as the 2nd smallest singular value in the straight flight case. Choosing the same threshold as in the straight flight case to determine the effective rank of the observability matrix, the matrix now has full rank, implying that the system is fully observable in turning. From Fig. 4c, we see that two out of six states depend on the smallest singular value, the east component of the wind and the ground speed. In the same way, the north component of the wind and the ground speed depend on the 2nd smallest singular value. As the two

TABLE I
SENSOR CHARACTERISTICS AND EKF PARAMETERS

	Value	**Unit**
Gyro noise density	3.0e-4	$\mathrm{rad}/(\mathrm{s}\sqrt{\mathrm{Hz}})$
Gyro bias noise density	1.0e-5	$\mathrm{rad}/(\mathrm{s}^2\sqrt{\mathrm{Hz}})$
Accel. noise density	1.0e-2	$\mathrm{m}/(\mathrm{s}^2\sqrt{\mathrm{Hz}})$
Accel. bias noise density	1.0e-4	$\mathrm{m}/(\mathrm{s}^3\sqrt{\mathrm{Hz}})$
Wind random walk density (range)	0.005 – 0.3	$\mathrm{m}/(\mathrm{s}^2\sqrt{\mathrm{Hz}})$
GPS position noise (NED) STD	[2.2, 2.2, 10]	m
Static pressure noise STD	9.5	Pa
Dynamic pressure noise STD	5.3	Pa

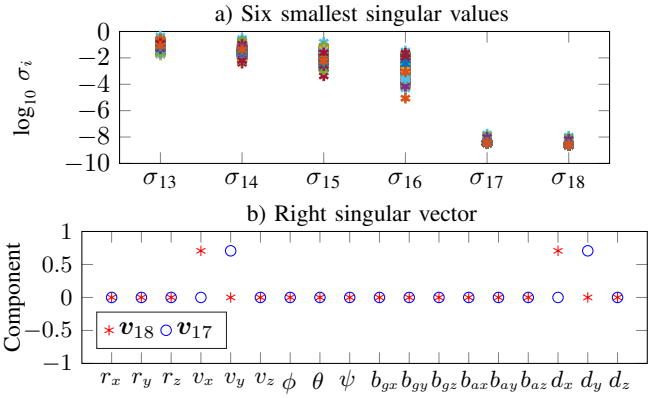

Fig. 5. SVD of the observability matrix for the full state model: a) six smallest singular values in logarithmic scale at different time instants, b) right singular vector $\boldsymbol{v}_{17}$ and $\boldsymbol{v}_{18}$ of the second smallest and smallest singular value, respectively.

smallest singular values are of the same order of magnitude, this implies that both directions of wind and ground speed can be equally well estimated in turning.

The fact that the observability matrix in turning has full rank, whereas it is effectively rank deficient in straight flight confirms the derived observability condition (22).

IV. Observability Analysis for Full State EKF

We apply the SVD based observability analysis to the full state EKF described in Section II. Differently to Section III-C, we use sensor signals recorded onboard of a glider with 18 m wingspan (ASG 29). As measurements, we use the angular rate, the acceleration, and the temperature from an MPU-9250, the position from a GPS receiver (u-blox 7), the static pressure from a barometer (MS5611-01BA03), and the dynamic pressure from a Pitot tube (MS4525DO). Table I shows the sensor characteristics and additional model parameters used in the EKF.

We apply the same procedure to calculate the observability matrix for the full state system as described in Section III-B by time-discretization of the continuous-time equations in Section II. Fig. 5a shows the 6 smallest of the 18 singular values at different time instants. The two smallest singular values are very close and in the same order between 10^{-8} and 10^{-9}. Fig. 5b shows their right singular vectors. Each of these singular vectors is related to the same component of the ground speed and of the wind. E.g., the north ground speed and the north wind speed have a nonzero entry in the right singular vector of the smallest singular value. This implies that the north and east components of the ground speed as

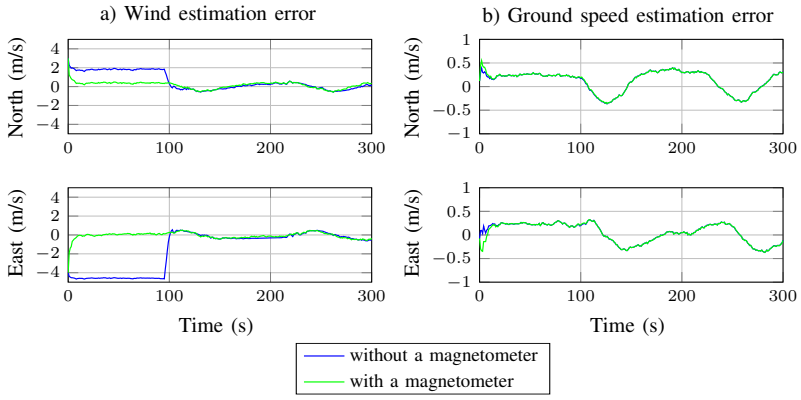

Fig. 6. Wind and ground speed estimation errors with and without a magnetometer based on simulated flight data.

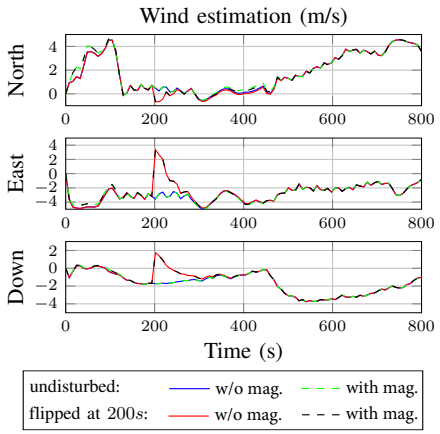

Fig. 7. Effect of a perturbation of the wind estimate and effect of adding a magnetometer based on recorded data.

well as of the wind speed have an independent impact on the observability matrix, as it has been also observed for the 2D simplified model in case of turning, see Fig. 4c. This highlights that the wind is observable for the full state system in real flights due to the random nature of the air mass causing a change in the direction of true airspeed. Differently to this, the analysis in Section III-C was based on the simulated flight with constant wind, i.e., the necessary random component that renders the system always observable in practical scenarios (even in straight flight) was missing.

V. Experimental Estimator Validation

A. Results of Simplified 2D Estimator

As the input of the 2D EKF, the sensor data are calculated based on the simulated flight trajectory, which is a ground truth [17], disturbed by additive white Gaussian noises. The simulated flight has a straight path from $0\,\mathrm{s}$ to $95\,\mathrm{s}$, and subsequently two banked turns. To compare the 2D EKF with the one with a magnetometer, we have included an ideal magnetometer impaired by additive Gaussian noise only. Fig. 6 shows the tracking performance for the wind and ground speed estimates. In the tracking mode even an ideal magnetometer negligibly little increases the accuracy. This suggests that using a real magnetometer impaired by unknown systematic and random disturbances in the full EKF is not meaningful. The EKF with a magnetometer has the advantage that it acquires lock even for a strictly straight flight path (no curvature). The EKF without a magnetometer quickly and reliably acquires lock only after a curvature of the flight path. This is in agreement with condition (22) given by the observability analysis.

B. Results of Full State Estimator

We tested the full state EKF using data recorded in an extensive series of test flights on a glider. The sensor settings are the same as in Section IV. Fig. 7 shows the effect of a perturbation of the wind estimate (direction flipped by $180°$). The wind estimate converges quickly to the undisturbed estimate. For comparison we used a magnetometer calibrated in the lab as additional sensor. As can be seen from Fig. 7 the estimates of the EKF with and without a magnetometer are practically identical after the EKF has acquired lock. During testing of the full state EKF without a magnetometer with several measurements taken on a series of flights, we never observed that the estimator loses track of the wind. This validates the finding that the full state EKF is effectively observable regardless of the flight patterns and, hence, the EKF works without a magnetometer independent of the flight pattern.

VI. Conclusion and Outlook

Using a simplified 2D model we have proven that the state is observable in case of a time-varying true airspeed direction while not using a magnetometer. This condition is fulfilled in practical scenarios. Moreover, a numerical observability analysis for the 2D EKF with simulated flight data (no randomness in the wind) shows that in straight flight the observability matrix is effectively rank deficient – one dimension of the wind vector remains unobservable – while in turning it has full rank. However, due to the random nature of the air mass, in a practical setting the state is observable independent of the flight pattern, as shown by the numerical observability analysis of the full state EKF based on measured data recorded onboard of gliders. This shows that the EKF works without a magnetometer. Finally, these results have been validated by an experimental performance evaluation of the EKF using measurement data recorded in numerous test flights. This shows that the EKF works and that the state estimates quickly converge to the undisturbed estimate after a perturbation.

While this observability analysis already gives detailed insight into the behavior of the EKF based flight state estimator, it does not explain its good tracking behavior experimentally observed, i.e., we never observed that the EKF loses lock. Thus, a study of the tracking behavior of the nonlinear EKF is the subject of an upcoming publication.

Acknowledgement

We are very grateful to LXNAV for providing data and avionics hardware, and sharing their in-depth knowledge on flight state estimation. We also gratefully acknowledge the very constructive criticism by the reviewers.

REFERENCES

[1] S. Leutenegger and R. Siegwart, "A low-cost and fail-safe inertial navigation system for airplanes," in *Proc. IEEE International Conference on Robotics and Automation*, Saint Paul, Minnesota, USA, May 2012, pp. 612–618.

[2] S. Leutenegger, A. Melzer, K. Alexis, and R. Siegwart, "Robust state estimation for small unmanned airplanes," in *Proc. IEEE Conference on Control Applications (CCA)*, Antibes/Nice, France, Oct. 2014, pp. 1003–1010.

[3] S. Leutenegger, "Unmanned solar airplanes - design and algorithms for efficient and robust autonomous operation," Ph.D. dissertation, ETH Zürich, Zürich, Switzerland, 2014.

[4] C. Eling, L. Klingbeil, and H. Kuhlmann, "Real-time single-frequency GPS/MEMS-IMU attitude determination of lightweight UAVs," *Sensors (Switzerland)*, vol. 15, no. 10, pp. 26 212–26 235, 2015.

[5] M. B. Rhudy, Y. Gu, J. Gross, and H. Chao, "Onboard wind velocity estimation comparison for unmanned aircraft systems," *IEEE Transactions on Aerospace and Electronic Systems*, vol. 53, no. 1, pp. 55–66, 2017.

[6] M. Brossard, J.-P. Condomines, and S. Bonnabel, "Tightly coupled navigation and wind estimation for mini UAVs," in *Proc. 2018 AIAA Guidance, Navigation, and Control Conference*, Kissimee, Florida, USA, Jan. 2018, p. 1843.

[7] R. Hermann and A. Krener, "Nonlinear controllability and observability," *IEEE Transactions on Automatic Control*, vol. 22, no. 5, pp. 728–740, 1977.

[8] A. Martinelli, "State estimation based on the concept of continuous symmetry and observability analysis: The case of calibration," *IEEE Transactions on Robotics*, vol. 27, no. 2, pp. 239–255, 2011.

[9] J. A. Preiss, K. Hausman, G. S. Sukhatme, and S. Weiss, "Simultaneous self-calibration and navigation using trajectory optimization," *The International Journal of Robotics Research*, vol. 37, no. 13-14, pp. 1573–1594, 2018.

[10] G. P. Huang, A. I. Mourikis, and S. I. Roumeliotis, "Observability-based rules for designing consistent EKF SLAM estimators," *The International Journal of Robotics Research*, vol. 29, no. 5, pp. 502–528, 2010.

[11] A. Barrau and S. Bonnabel, "An EKF-SLAM algorithm with consistency properties," Oct. 2015. [Online]. Available: https://arxiv.org/abs/1510.06263

[12] J. Stigter, D. Joubert, and J. Molenaar, "Observability of complex systems: Finding the gap," *Scientific reports*, vol. 7, no. 1, p. 16566, 2017.

[13] J. Solà, "Quaternion kinematics for the error-state Kalman filter," Nov. 2017. [Online]. Available: http://arxiv.org/abs/1711.02508

[14] P. D. Groves, *Principles of GNSS, inertial, and multisensor integrated navigation systems*. Artech house, 2008.

[15] D. A. Caughey, "Introduction to aircraft stability and control course notes for M&AE 5070," *Sibley School of Mechanical & Aerospace Engineering Cornell University*, 2011.

[16] W. J. Rugh, *Linear System Theory*. Upper Saddle River, NJ, USA: Prentice-Hall, Inc., 1996.

[17] R. Dilão and J. Fonseca, "Dynamic trajectory control of gliders," in *Advances in Aerospace Guidance, Navigation and Control*. Springer, 2013, pp. 373–386.

[18] G. Strang, *Introduction to linear algebra*. Wellesley-Cambridge Press Wellesley, MA, 2006, vol. 4.